ACS APPLIED MATERIALS & INTERFACES

Forum Article

www.acsami.org

Study of Osteoclast Adhesion to Cortical Bone Surfaces: A Correlative Microscopy Approach for Concomitant Imaging of Cellular Dynamics and Surface Modifications

Michal Shemesh,[†] Sefi Addadi,[‡] Yonat Milstein,[‡] Benjamin Geiger,[§] and Lia Addadi*[,†]

[†]Department of Structural Biology and [§]Department of Molecular Cell Biology, Weizmann Institute of Science, 76100 Rehovot, Israel
[‡]B-Nano Ltd., 76326 Rehovot, Israel

Supporting Information

ABSTRACT: Bone remodeling relies on the coordinated functioning of osteoblasts, bone-forming cells, and osteoclasts, bone-resorbing cells. The effects of specific chemical and physical bone features on the osteoclast adhesive apparatus, the sealing zone ring, and their relation to resorption functionality are still not well-understood. We designed and implemented a correlative imaging method that enables monitoring of the same area of bone surface by time-lapse light microscopy, electron microscopy, and atomic force microscopy before, during, and after exposure to osteoclasts. We show that sealing zone rings preferentially develop around surface protrusions, with lateral dimensions of several micrometers, and ∼1 μm height. Direct overlay of sealing zone rings onto resorption pits on the bone surface shows that the rings adapt to pit morphology. The correlative procedure presented here is noninvasive and performed under ambient conditions, without the need for sample labeling. It can potentially be applied to study various aspects of cell-matrix interactions.

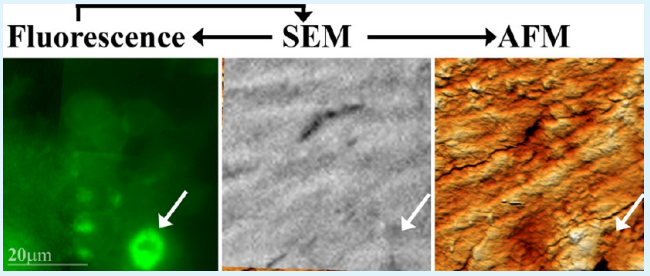

KEYWORDS: *AFM, airSEM, bone, osteoclasts, resorption, sealing zone dynamics, CLEM*

INTRODUCTION

The adaptation of bone tissue to the physical, chemical, and biological stimuli to which it is continuously exposed occurs through the coordinated activity of bone-forming cells, the osteoblasts, and bone-resorbing cells, the osteoclasts. Bone is thus incessantly renovated and remodeled. Loss of balance between bone resorption and deposition can lead to impaired bone strength and flexibility, as well as to the malfunction of other related tissues.[1] This complex remodeling process is extremely sensitive to the local environment in which cells are operating.[2−7] Communication between osteoclasts and osteoblasts, as well as with other cells such as osteocytes, regulates the remodeling process. Regulation occurs at several levels, involving osteoclastogenesis, stimulated by osteocyte signaling, in specific areas of damage,[8−10] and coordinated osteoblast deposition of new bone matrix within exposed resorption lacunas.[11−13] As a result of these activities, cortical bone displays a hierarchical, multiscale complexity:[14] at the submicron scale, mineralized collagen fibrils are arranged as 3−5 μm thick lamellae that, at a higher hierarchical level, fold around haversian canals in an osteonal structure.[15]

The primary adhesion units in osteoclasts are podosomes, actin-based structures composed of proteins similar to those found in focal adhesions.[16] Podosomes display a distinct architecture, consisting of a central core of tightly packed actin filaments oriented perpendicular to the ventral membrane, surrounded by a membrane-bound adhesion plaque comprising integrins and adhesion proteins.[17−22] In differentiated osteoclasts, individual podosomes assemble to form sealing zone (SZ) rings, delimiting the area into which protons and proteases are secreted to digest the underlying matrix. The resorptive function of osteoclasts was shown to depend on their adhesion to the bone surface through the SZ[17,23] and to correlate with substrate degradation and uptake.[19,24−26] However, the direct connection between osteoclast SZ dynamics and resorption has yet to be unraveled.

The SZ superstructure is highly sensitive to extracellular matrix (ECM) parameters and differs among osteoclasts adhering to different surfaces. In particular, the effect of surface topography on SZ formation and development has been studied on artificial substrates such as calcite, titanium, or nacre.[27−30] SZ structures were shown to adapt to the three-dimensional architecture of the surface, within a range of micrometers to tens of micrometers.[27,29] In bone implants, surface nano and micro roughness was shown to affect cell attachment and differentiation into osteoblasts.[30,31]

Special Issue: Current Trends in Functional Surfaces and Interfaces for Biomedical Applications

Received: August 31, 2015
Accepted: December 8, 2015

DOI: 10.1021/acsami.5b08126
ACS Appl. Mater. Interfaces XXXX, XXX, XXX−XXX

Local surface chemistry also affects SZ development and osteoclast resorption, as osteoclasts favor adhesion to mineral[32−34] and resorb it faster than the organic components of bone.[35,36] Noncollagenous proteins, which are bound to bone mineral and released during resorption,[37,38] regulate both bone resorption and deposition processes.

The size, stability, and dynamics of SZ rings are also surface-dependent: on glass surfaces, incomplete, highly unstable rings form at the cell periphery. On calcite, rings tend to fuse and form a stable peripheral ring, with a lifespan of several hours. On bone, in contrast, small and stable SZ rings with lifespans of several hours form at specific locations underneath the cell body. The question then arises: Why do stable rings form at specific locations, rather than in neighboring areas underneath the same cell? Several factors may contribute to this phenomenon, including local differences in bone surface chemistry, topography, and organic content.[39] A second issue of interest concerns the connection between surface modification by osteoclasts and the characteristics of the specific SZ ring juxtaposed onto it.

To address these, and potentially many other related questions, we seeded differentiated osteoclasts on bone surfaces and examined the dependence of osteoclast adhesion, dynamics, and resorption activity on local bone surface features. For this purpose, the tracking of individual SZ rings from the initial adhesion of the osteoclast to the bone surface must be undertaken within the context of local bone characterization. This requires the development of a fully correlative method, enabling precise observation of both the bone and the attached cells during interaction. The main difficulty consists in achieving simultaneous imaging of dynamic subcellular processes and surface morphology, at adequate spatial and temporal resolution. Furthermore, the bone samples must be kept wet throughout the different stages of the experiments, because water is an essential component of bone, and its removal causes irreversible modification of bone structure and chemistry.

In the past, correlative imaging was achieved using elegant combinations of different techniques, providing information that could not be obtained with any individual technique.[40−44] These correlative techniques were not applicable in our case, since we needed an accurate overlay of very different images: the actin rings formed in the cells, and the opaque bone surface, which displays no obvious structural surface motifs at the same order of magnitude as the SZ.

We therefore developed a procedure combining high-resolution scanning electron microscopy (SEM) and atomic force microscopy (AFM), conventionally used to characterize bone morphology and resorption[45−50] with fluorescence live imaging of SZ rings in cells.[18,27] We then applied this technique to image bone-resorbing osteoclasts at different stages of their adhesion to cortical bone surfaces.

MATERIALS AND METHODS

Correlative Microscopy Workflow. Step 1 (Scheme 1): Fresh bone slices were prepared and placed inside a specially designed holder (Step 2). Step 3: The entire surface was imaged with the airSEM. Step 4: GFP-actin-tagged RAW 264.7 cells were transferred from the differentiation Petri dish to the bone surface. Step 5: Time-lapse fluorescence movies of SZ dynamics in real time were taken with a Delta Vision inverted microscope. Step 6: Cells were fixed, and the bone sample was transferred to the airSEM. Here, the samples were first imaged

Scheme 1. Correlative Microscopy Workflow

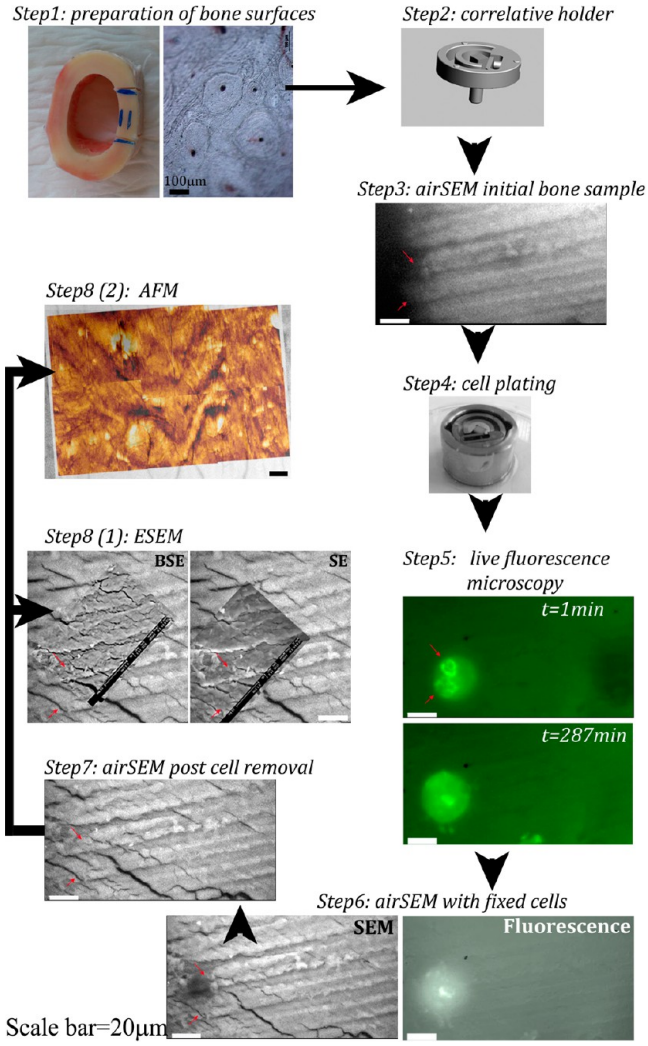

under the fluorescence microscope, to enable their correlation with the optical images from the Delta Vision, and then with the electron microscope, at exactly the same locations. Step 7: Cells were removed, and the bone surface was imaged in the electron microscope, again at exactly the same bone locations. Step 8: The bone samples, still inside the holders, could then be taken either to the environmental SEM (ESEM) or the AFM, to further characterize specific locations of interest. Finally, the individual images were stitched, overlaid, and correlated individually by hand, exploiting, for the purposes of alignment, bone surface features visible in all images, though taken at different steps. A detailed description of each step follows.

Step 1: Preparation of Bone Surfaces for Correlative Microscopy. Fresh (less than 1 d post-mortem), young (less than one year-old) cattle femur was obtained from a local butcher shop (Moo&Moo, Rehovot, Israel). To prevent cumulative damage to the bone surface, all the correlative procedures prior to cell removal were completed within one week post-mortem.

Thin (3 × 3 × 2 mm) slices showing osteonal arrangement of the mineralized collagen bundles were cut from the femur mid area (between the anterior and posterior sides, see scheme), using a low-speed diamond saw (South Bay Technology, Inc., San Clemente, CA, USA).

DOI: 10.1021/acsami.5b08126
ACS Appl. Mater. Interfaces XXXX, XXX, XXX−XXX

Step 2: Design of the Correlative Bone Holder. A stainless steel 316 (SS316) holder was specifically designed to correlate between electron and optical microscopes (Instrument designer: Pasmantirer Benjamin; Manufacturer: Scientific Instrumentation, Research Services Division, Weizmann Institute of Science, Israel). Bone specimens are washed briefly with ethanol 70% for sterilization and placed inside the holder, where they are held in place by a lever, with an applied force calculated to prevent movement during the different stages of the experiments, and avoid deformation of the bone. The bone specimen is immersed in a pool of cell culture medium, to prevent dehydration. Bone specimens remain in the holder throughout the experimental cycle, with no change in location.

Step 3: Imaging the Initial Bone Sample Prior to Cell Plating. Bone specimens were imaged by means of an airSEM (B-Nano, Ltd., Rehovot, Israel) imaging station, consisting of an SEM capable of producing images up to a resolution of 50 nm in air under ambient conditions, without the need to pretreat the sample. The bone was maintained constantly hydrated during imaging, with medium provided from the holder pool. The bone surface was mapped by sequential images with a 480 μm field of view (FOV) and overlap of 50 μm, using automated stage coordination. All stage movements were computer-controlled. The detected signal consisted of backscattered electrons; beam energy was 30 kV, and probe current was 500 pA.

Step 4: Tissue Culture, Differentiation, and Cell Transfer to Bone. RAW 264.7 cells stably expressing GFP-actin[51] were obtained from the American Type Culture Collection (ATCC; Manassas, VA, USA), cultured in DMEM with Earl's salts, 1% L-glutamine, and $NaHCO_3$ and supplemented with fetal bovine serum (FBS; 10%; Gibco, Grand Island, NY, USA) and antibiotics (1% pen-strep; Biological Industries, Beit Haemek, Israel). For osteoclast differentiation, RAW cells were cultured on plastic dishes (100 cells/mm^2) in α-MEM with Earle's salts, L-glutamine, and NaHCO3 (Sigma, Rehovot, Israel), supplemented with FBS and antibiotics, 20 ng mL^{-1} recombinant soluble receptor activator of NFkB ligand, and 20 ng mL^{-1} macrophage colony-stimulating factor (R&D Systems) at 37 °C in a 5% CO_2 humidified atmosphere for 60 h. Differentiation medium was changed every 24 h. Once differentiated, cells were removed with ethylenediaminetetraacetic acid (10 mM) for 10 min, centrifuged, resuspended in differentiation medium, and transferred to the bone surface. Prior to cell plating, bone surfaces were conditioned with vitronectin (10 μg/mL) for 10 h at 4 °C, then washed three times with culture medium, and heated to 37 °C.

Step 5: Live Fluorescence Microscopy. For time-lapse movies, differentiated osteoclasts that had been transferred to the bone surfaces were allowed to adhere for 1 h. The holder containing bone with suspended cells and culture medium was placed inside a specially designed cup (SS316) with slots in its upper section, enabling the transfer of CO_2 to the cells. The cup was covered with a standard Petri dish cover and placed in a humidified atmosphere (37 °C at 5% CO_2). After 1 h, the holder was placed upside-down on a MatTek glass-bottomed dish (No. P35G-0−20-C, MatTek Corp., Ashland, MA, USA). Time-lapse images were acquired with an automated inverted microscope (DeltaVision Elite system IX71 with Resolve3D software modulus; Applied Precision, Inc., GE Healthcare, Issaquah, WA, USA) using a 20×/0.85 oil objective (Olympus, Tokyo, Japan). The microscope is equipped with an environmental box kept at 37 °C with a 5% CO_2 humidified atmosphere. Images were acquired every 1 min or every 30 s, for up to 6 h. Following time-lapse imaging, cells were fixed and stained for actin and nuclei. For fixed-sample imaging, samples were collected at chosen time periods (3, 6, 24, and 48 h) post-transfer to the bone surface, permeabilized with 0.5% Triton X-100 (Fluka-Chemie AG, Switzerland), and fixed in warm 3% paraformaldehyde (Merck, Darmstadt, Germany). Postfixation, specimens were washed three times with PBS and stained for actin (FITC-phalloidin, Sigma) and nuclei (Hoechst 33342 Life Technologies, Thermo Fisher Scientific Corp., Carlsbad, CA, USA). The entire bone surface, including the stained cells, was imaged with the Delta Vision RT microscope (Applied Precision), using a 20×/0.85 oil lens. Images with a FOV 330.24 × 330.24 μm were stitched using Adobe Photoshop software and aligned to the SEM images. Image analysis was performed using ImageJ software.[52]

Step 6: Imaging Bone Specimens Post Cell Interaction. Fixed and stained cells on the bone specimens were imaged with the epifluorescence setup connected to the airSEM, at locations near the bone edges; these images were then compared with images from the DeltaVision optical microscope to achieve image correlation. Bright-light and epifluorescence images were obtained using the imaging station of the upright airSEM microscope, equipped with 5× (MPLNX/0.1) and 40× (MPLNX/0.75) air objectives and standard filter cubes, DAPI [Ex′: BP330−385; Em ′:BA420], and Cy3 [Ex′ BP530−550; Em′ 575−625] for epifluorescence.[53] The sample was then shuttled under the electron microscope, and SEM images of the bone surface with osteoclasts still attached were taken at the same locations imaged by the optical microscope.

Step 7: Imaging Bone, Post Cell Removal. For cell removal, a droplet of sodium hypochlorite (NaOCl 6%; Bio-Lab, Ltd., Jerusalem, Israel) was gently applied to the bone surface and was washed after 15 min with doubly distilled water × 3. The water was removed, and the bone was gently dried with a nitrogen stream. The entire procedure was performed with the bone in the holder on the stage of the airSEM imaging station. In this manner, the coordinates of images prior to and following cell removal could be correlated. The entire bone surface was imaged in this manner.

Energy dispersive X-ray spectroscopy (EDX) composition analysis was also performed on the bone samples. The airSEM system is equipped with an EDX detector (Quantax, Xflash 630, Bruker, Germany), enabling analysis of local material composition and elemental mapping of the different sample constituents (Figure S1).

Step 8: Environmental SEM Imaging. For higher resolution, and comparison of the back scattered electrons (BSE) signal to the secondary electrons (SE) signal, the bone specimen, after cell removal and still inside the holder, was taken to the ESEM (XL 30 ESEM-FEG Philips/FEI), where certain areas of interest were imaged at 20 kV, under vacuum conditions (0.7 Torr). The location of specific areas of interest in the bone surface was determined by triangulation between the positions relative to the holder edges and by comparison to the airSEM images. Both backscattered and secondary electron images were taken and compared.

Step 9: Atomic Force Microscopy. A JPK NanoWizard 3 (JPK Instruments, Berlin, Germany) equipped with an upright optical microscope (Axiozoom v16, Carl Zeiss Microscopy GmbH, München, Germany) was used to image bone surfaces

DOI: 10.1021/acsami.5b08126
ACS Appl. Mater. Interfaces XXXX, XXX, XXX−XXX

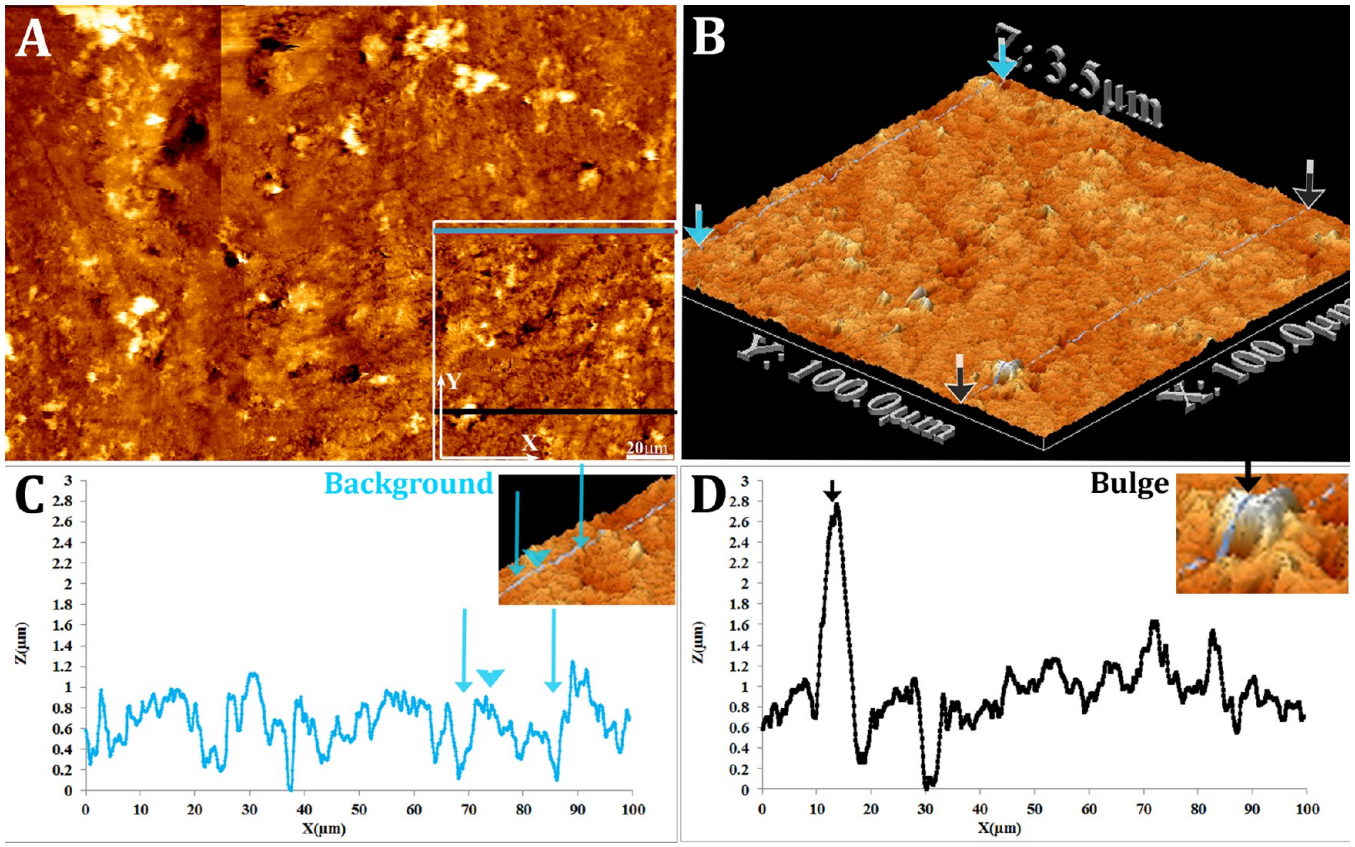

Figure 1. Bone surface following sawing and prior to cell transfer, imaged with an AFM. (A) Stitched images of a representative bone surface area, demonstrating the variety of topographies present on the surface. Within the boxed area, the blue line represents the location of the height profile in (C) taken in correspondence to a region of background topography, whereas the black line represents the location of the height profile in (D) correspondence to a region with a representative bulge on the surface. Scale = 20 μm. (B) 3D representation of the boxed area in (A), demonstrating the height differences on the surface. Blue arrows point to the edges of the background profile in (C), and black arrows point to the edges of the bulge line profile in (D). (C) Line profile taken from the original height image in the location of the blue line in the boxed area in Panel (A). (inset) The magnified area from the 3D representation in Panel (B). Grooves delimiting ridges due to saw markings are marked by blue arrows. The ridges have width of 15.5 ± 1.0 μm and height of 0.9 ± 0.1 μm. At a smaller scale, protrusions are emerging all over the surface (blue arrowhead), and have typical width of 1 μm and heights within a range of 0.1−0.6 μm. (D) Line profile taken from the original height image in the location of the black line in the boxed area in Panel (A). (inset) The magnified area from the 3D representation in Panel (B). A representative bulge on the surface (black arrow) has width of 7.5 μm and height of 1.6 μm.

prior to or following cell interaction. Pyramidal silicon nitride triangular cantilevers (DNP; Bruker Corporation, Camarillo, CA), with a nominal stiffness of 0.12 N/m and a nominal radius of 20 nm, were used. Prior to cell transfer, the bone surface was imaged in liquid (cell cultivation medium) in contact mode, set point = 2 V, line rate = 0.7 Hz, and I Gain = 100 Hz. Images with a scan size of 100 μm each were taken in adjacent locations and viewed in the overview window using the JPK image processing software. Height profiles (from the original height image, subjected to plane fitting to remove sample tilt) and three-dimensional (3D) images were taken using WsXM software.[54] Following cell removal, the bone surface was imaged in air, in contact mode. The bone sample was kept in the holder, which was placed inside a Petri dish appropriately adapted to enable upright imaging of the surfaces, without limiting cantilever movement. Parameters: Set point = 0.6 V; line rate = 0.7 Hz; and I Gain = 130 Hz. Height profiles and 3D images were computed using WsXM software.

Image Correlation. The orientation of the holder was kept constant in all microscopes. The stage movements and relative distances between areas of interest were performed via computer-controlled stages, which minimized the possibility of error (see Step 3). Stitching of the individual images was performed manually, using Adobe Photoshop CS4 software, after equalizing brightness and contrast levels and overlaying common surface features. Accurate correlation of the images was achieved by overlaying them according to anchor points on the bone surface, such as microcracks or mineral aggregates, osteocyte lacunae, and bone edges, visible in the images acquired by the different techniques. These features are directly visible in the SEM images and were made visible in the fluorescence images by taking additional frames with increased exposure in selected anchor locations or by increasing the brightness after acquisition. Correlation of SEM images (upright configuration) with optical images (inverted configuration) required further image mirroring. Correlation between airSEM and the ESEM BSE images was straightforward, due to similarities in the surface signals. For the same reason, AFM surface images could be correlated with surface features imaged by the SEM, after tilt and magnification corrections.

RESULTS

1. The Design of a Microscopy Setup, Enabling Use of the Correlative Light-Electron Microscopy (CLEM)

DOI: 10.1021/acsami.5b08126
ACS Appl. Mater. Interfaces XXXX, XXX, XXX−XXX

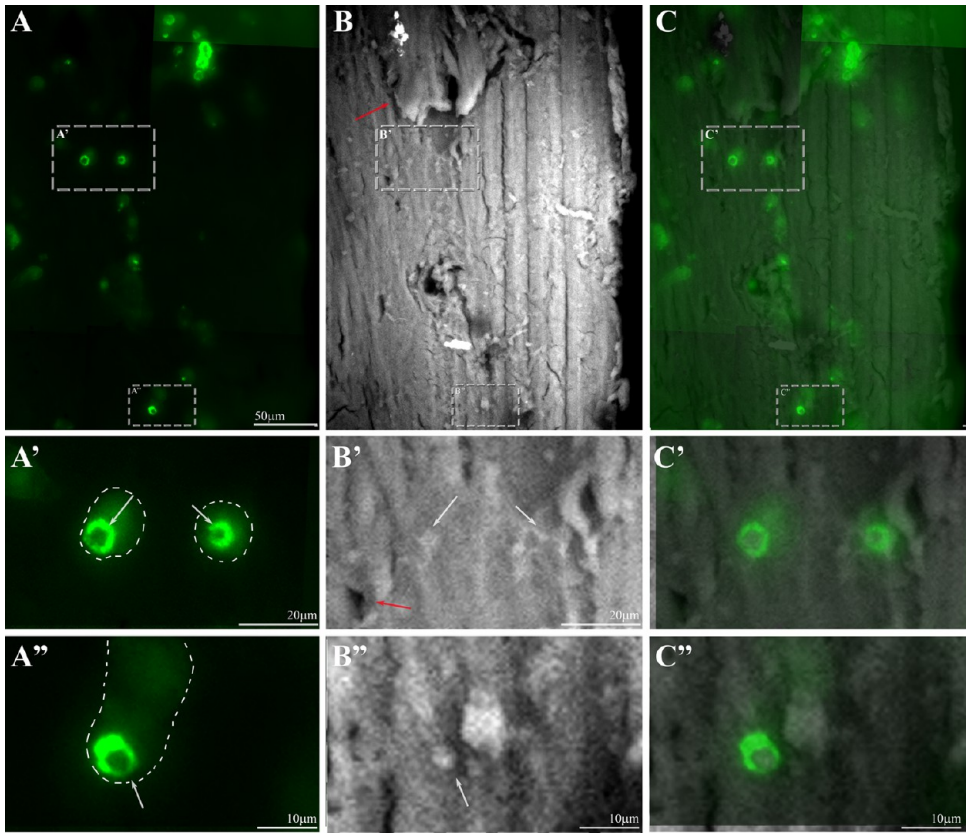

Figure 2. SZ rings in correlation to bone surface features. (A) Stitched fluorescence image of GFP-actin, showing SZ rings 3 h postosteoclast transfer to the bone surface. The three SZ rings in boxed areas are magnified in (A′, A″). (B) The corresponding airSEM image of the bone surface. Saw markings decorate the surface; in the upper part of the image, an exposed canal emerges from the surface (red arrow); microcracks can be seen in different locations. (C) Overlay correlating the fluorescence to the SEM images, showing the adaptation of SZ rings to the bone surface. (A′, B′, C′) Magnification of the area in the upper rectangle: Two SZ rings formed, surrounding small bulges present on the bone surface. White arrows denote ring locations, and the cell borders are marked by dashed white lines; the red arrow denotes an osteocyte lacuna nearby. (A″, B″, C″) Magnification of the area in the lower rectangle: An SZ ring formed (A″, white arrow), surrounding a small bulge on the surface (B″, white arrow). The cell border is marked by a dashed white line. Scale bars: A = 50 μm; A′ = 20 μm; A′′ = 10 μm.

Approach. To image the same bone surface area with different techniques, images must be successfully overlaid at accuracy better than 1 μm. In addition, the bone samples must be kept wet throughout the different stages of the experiment to avoid modification of bone structure and chemistry. To meet these requirements, we designed a specialized holder, in which a fresh cut bone slice is securely positioned throughout the entire process, with no external modifications.

Conventional SEM is performed under vacuum and thus requires drying of the specimens, a process incompatible with the later, live-cell imaging stage. The airSEM imaging station is based on a new SEM technology that operates in air under ambient conditions, providing sample imaging and elemental analyses. A translation stage connects the SEM to an optical microscope, providing fully correlated SEM and bright light or fluorescence images.[55] Data acquired on wet bone surfaces in this configuration using the optical microscope with resolution of up to 0.5 μm can thus be related to surface features imaged in the airSEM at the same resolution. In turn, the epifluorescence correlates with the higher resolution static and dynamic images from the Delta Vision system (resolution of up to 200 nm), and the airSEM correlates with images taken with higher resolution ESEM techniques after cell removal and specimen drying (up to 100 nm), or with the AFM (with lateral resolution up to 50 nm, and height resolution up to 5 nm under the present working conditions). At the end of the experiment, dried samples can be observed with high-resolution SEM (up to 5 nm resolution, S2).

The flowchart of the operations is described in detail in Materials and Methods section and in Scheme 1. Briefly, bone samples were imaged with the airSEM, prior to cell plating. Once cells were plated, SZ dynamic behavior was tracked by live time-lapse fluorescence microscopy. Samples were then fixed and returned to the airSEM, where they were imaged at selected areas of interest by fluorescence and electron microscopy, both prior to and following cell removal. Finally, ESEM and/or AFM were used to image resorbed areas at high resolution.

2. Adaptation of Sealing Zone Structures to Bone Surface Topography. AFM in contact mode under liquid (osteoclast buffer) was performed on longitudinal sections of fresh cattle femur osteonal bone (see Step 1 in Materials and Methods and Scheme 1). Longitudinal sections were chosen because they expose surface areas that correspond to the direction of load and to the main direction of osteoclast resorption, forming haversian canals mostly parallel to the axes of the long bones.[56−58]

A typical AFM image of a saw-cut bone surface displays multiple topographies (Figure 1A,B), among which we focus on three characteristic features within the relevant range: repeating

DOI: 10.1021/acsami.5b08126
ACS Appl. Mater. Interfaces XXXX, XXX, XXX−XXX

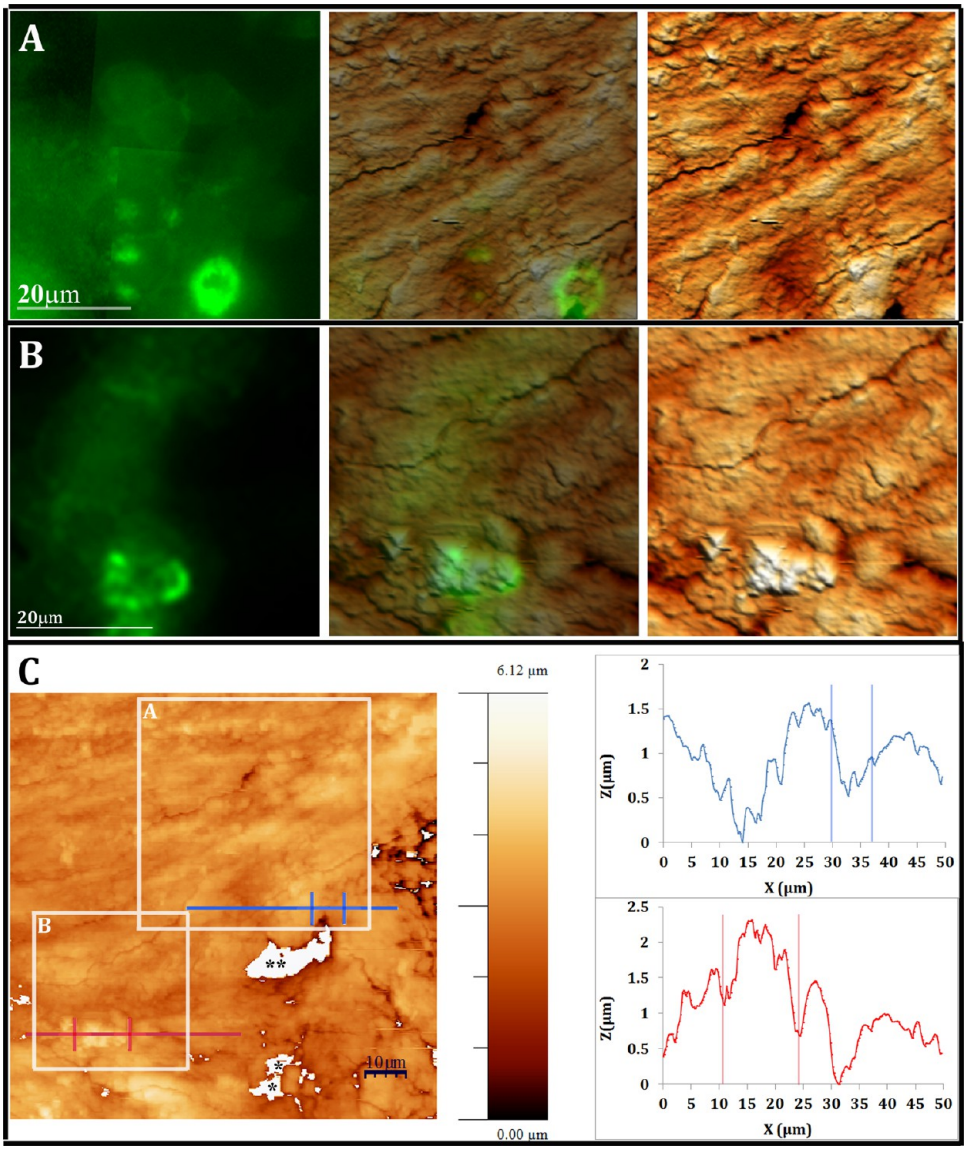

Figure 3. SZ rings imaged with a fluorescence microscope correlated with 3D topographic AFM images of bone surface taken after cell removal. (A, left) Fluorescence. (A, right) AFM 3D representation. (A, middle) Overlay. SZ ring with a diameter of 8 μm adapting to the bone surface topography. (B, left) Fluorescence. (B, right) AFM 3D representation. (B, middle) Overlay. Elongated SZ ring, with a 13 μm diameter in the long axis, surrounds a protrusion on the bone surface. (C) AFM height image of the bone area from which 3D images were produced (boxed areas). Asterisks note deep depressions on the surface. Line profiles represent surface topography beneath the SZ rings shown in (A, blue) and (B, red); the differences in surface peak height beneath SZ rings are 0.7 μm (A, blue line) and 1.3 μm (B, red line).

pattern of ridges due to the saw markings have characteristic widths = 15.5 ± 1.0 μm (N = 21) and heights of 0.9 ± 0.1 μm; the distance between ridges is 3.5 ± 0.3 μm (N = 19); background small protrusions are present everywhere, their widths ranging ∼1 μm, and heights ranging between 0.1 and 0.6 μm (Figure 1A,C blue line). Larger bulges with widths ranging between 5 and 20 μm and heights ranging from 1 to 2 μm are more sparsely distributed over the surface (Figure 1A,D black line)

SEM images of the bone surface were taken with a 3 × 3 mm FOV (the entire specimen surface), to track and compare multiple adhesion events in different areas. We chose to monitor osteoclasts fixed 3 h post-transfer to the bone surface, because they do not have sufficient time to substantially alter the surface, although SZ rings are formed within an hour of cell plating (Supporting Information, Figure S3). Figure 2 shows a fluorescence image (A, A′, and A″) of the same location on the bone surface as imaged by the airSEM prior to cell plating (B, B′, and B″). The same ridge markings and bulges that were measured by AFM are clearly identifiable in the SEM images. Large structural elements (possibly part of a canal exposed during sawing), osteocyte lacunas, and small cracks emerge at various locations on the surface. Out of this topographic variety, the majority of SZ rings that were observed in connection to surface features are formed around bulges that match the more sparse and more protruding bulges observed by AFM (Figure 2C,C′,C″)

AFM imaging of the bone surface post cell removal shows that such SZ rings adapt in shape and size to surface geometry (Figure 3A,B). The height of the bulge delimited by the ring in Figure 3C is 1.3 μm, falling within the range characteristic of the sparser bulges measured in Figure 1.

Osteoclasts that were allowed to adhere to the bone surface for 24 h (Figure 4) have sufficient time to migrate on the bone

DOI: 10.1021/acsami.5b08126
ACS Appl. Mater. Interfaces XXXX, XXX, XXX−XXX

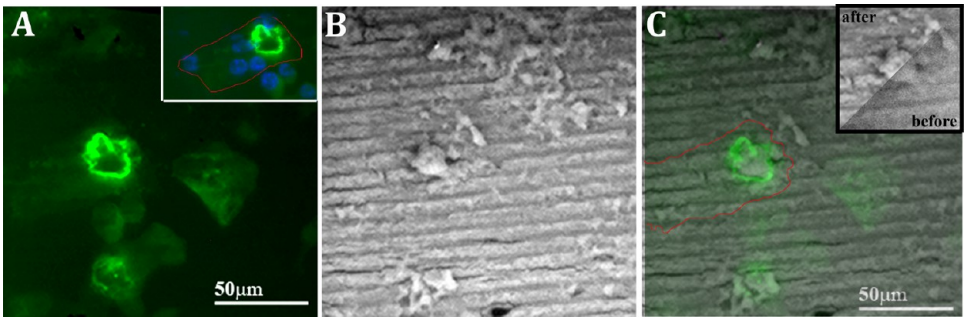

Figure 4. SZ rings in osteoclasts plated on bone surface for 24 h. (A) Fluorescence image of SZ ring (green) in cell fixed 24 h post transfer to the bone surface. (inset) Overlay of actin (green) and nuclei (blue). Scale: 50 μm. (B) airSEM image of the same bone area following cell removal. (C) Overlay of the ring image with the SEM image of the surface. For clarity, cell body area is demarcated with a red line. Notice that although the cell covers a larger area, the ring forms around an 18 μm bulge on the surface, adapting to its shape. (inset) A comparison of the surface bulge before and after osteoclast interaction with the surface, demonstrating that the bulge was not altered by the cell.

surface, giving them the possibility to search for selective features and answer to specific signals. The formation of SZ rings around surface bulges was a predominant phenomenon also at this time point, as observed at shorter time points. Likewise, we rarely, if at all, observed SZ rings in proximity to osteocyte lacunae, saw markings, or surface cracks.

The average size of the bulges around which SZs were observed at both time points (3 or 24 h) is 7.5 ± 1.2 μm (N = 20). This size well matches the size of the sparsely distributed larger bulges measured by AFM (Figure 1). Sealing zones were not observed around any of the smaller but much more frequent background protrusions.

We note that in fixed samples, no information is preserved on dynamic processes that ended prior to fixation. Therefore, short-lived SZ rings may have transiently formed in different locations and then dissolved or translocated.

3. Effect of Bone Surface Topography on the Dynamics of SZ Rings. To obtain information connecting the first steps in osteoclast adhesion through SZ formation and ring lifespan to bone surface structure and its modification, we tracked live cells on bone surfaces, utilizing live time-lapse fluorescence imaging of GFP-actin. Images were taken at 1 min intervals or less, to enable tracking of the fine dynamic cycles of SZ rings. SEM imaging of bone surfaces was performed prior to cell plating. Dynamic live imaging began 1 h post cell transfer to bone, enabling tracking of the complete history of rings at certain locations, and terminated after maximum of 6 h, to limit the chances for sequential ring formation at the same location. These time periods allow connecting between specific surface features and their degree of modification to a specific SZ ring with known characteristics.

A comparison of neighboring rings under the same stationary cell shows differences in their dynamic behavior (Figure 5): small dynamic rings repeatedly appeared and faded in the same location with a periodicity of several minutes, whereas a stable ring located in close proximity maintained its size throughout the entire movie. An area with more complex ring dynamics showed fusion and fission of rings, with variations in signal intensity along the ring perimeter, suggesting different actin concentrations (for the complete dynamics, see Supporting Information, Movie). Toward the end of the time-lapse movie, the rings began to translocate, and the movie was stopped.

Correlations between fluorescence and SEM images of the bone surface prior to cell plating (Figure 5B) show that the stable ring was formed around a surface bulge with diameter of 5.9 μm, whereas the more dynamic rings were formed on topographic edges. Comparison to the same area imaged by SEM post cellular interaction, with the cell still attached (fixed as is, with no NaOCl application; Figure 5E) shows that the area beneath the stable ring was altered, most likely by the cell itself. Several cracks on the bone surface, which were partially covered by organic material at the beginning of the movie, became more visible at the end of the movie, possibly because the bone partially dehydrated, following cell fixation. After cell removal with NaOCl, the surface area of interest, with the altered bulge, remained the same, and the cracks became wider (Supporting Information Figure S4).

In agreement with the observation made on fixed cells, the dynamics observed here support the notion that not only rings are preferentially formed around bulges of a certain size, but are also stabilized by them. This stabilization may eventually favor resorption.

4. Correlation between the Sealing Zone and Local Resorption of Bone Surface. By means of the correlative method, we could directly connect resorption pits on bone surface to SZ rings. For imaging the general morphology of the large pits operating the airSEM at medium magnification was sufficient (Figure 6). To image more subtle surface modifications, a conventional SEM with high resolution is more suitable, as it can reveal resorption in greater detail of the surface, following cell removal and sample dehydration (Supporting Information Figure S5).

Osteoclasts cultured for 24 h on bone developed SZ rings that correlated well with the characteristic resorption pits (Figure 6A), matching their diameter (31 μm) and shape. The pits did not exist prior to cell interaction with the bone (compare Figure 6B to Figure 6C). Similar SZ rings and resorption pits can be seen after cells were cultured on bone for 48 h (Figure 6D,E). The pits can also be seen through the cell body, prior to cell removal (Figure 6F). Our preliminary analyses indicated that 24 h after initial cell plating, a 3 × 3 mm area of bone surface contained tens of cells; each developed multiple rings of various sizes. However, none of the SZ rings with smaller diameters that that are formed around surface bulges were seen in the vicinity of resorption pits.

Correlations between resorption pits and SZs were not observed for cells that adhered to the surface for 6 h or less. However, in contrast to cells plated for that amount of time, for which specific SZ rings could be directly correlated with the underlying surface features, over a period of 24 h or more, the cells could migrate on the bone surface, and the dynamic SZ rings could expand, fuse, or translocate. As a consequence, at

DOI: 10.1021/acsami.5b08126
ACS Appl. Mater. Interfaces XXXX, XXX, XXX−XXX

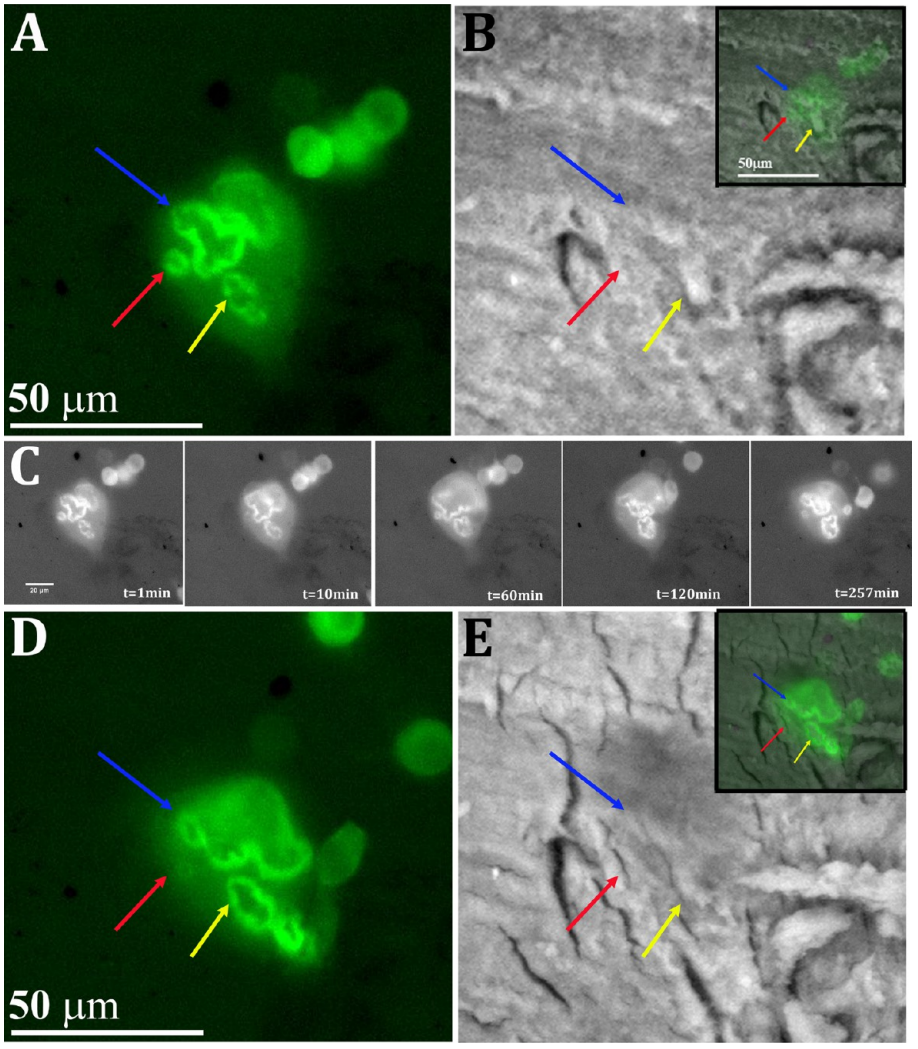

Figure 5. Relating ring dynamics to bone surface features. (A) The first time point from a time-lapse fluorescence movie; frames were taken at 1 min intervals; overall monitoring time was ~6 h. The small ring denoted by a red arrow is highly dynamic: with an overall lifespan of a few minutes, sequential rings form and disappear at different time points at the same location. The ring denoted by a yellow arrow persists throughout the monitored period. The ring denoted by a blue arrow undergoes cycles of fission and fusion during the imaging period. (B) airSEM image of the corresponding surface prior to cell plating. (inset) An overlay of the rings at the beginning of the movie. Notice the bulge around which the stable ring (yellow arrow) is formed. (C) Individual frames from the time-lapse movie, demonstrating differences in dynamic behavior of the rings. (D) Toward the end of the time-lapse movie (time point = 345 min): the dynamic ring (red arrow) fades, whereas the stable ring (yellow arrow) is still visible. (E) airSEM image of the bone surface after movie termination, with the fixed osteoclast cell still present (appearing as a shadow on the surface). (inset) An overlay of ring and surface images, at the end of the movie. Notice that the lower, stable part of the large ring (blue arrow) leans on the surface curvature, adapting to its shape. A comparison between (B) and (D) shows that the bulge beneath the stable SZ ring (yellow arrow) is altered. In addition, microcracks that are hardly visible at the beginning of the movie are more visible at the end. Scale = 50 μm.

both 24 and 48 h time points, some of the pits correlate with SZ ring size and shape, whereas other pits are seen in the vicinity of the rings but do not directly correlate with them.

DISCUSSION

Here, we presented the design, implementation, and power of a fully correlative imaging method that combines live monitoring of cell dynamics with high-resolution imaging of the substrate. Our goal here was to draw connections between subcellular osteoclast structures (mostly, the SZ), their response to specific surface features when adhering to it, and their function in modifying the underlying surface.

In general, the interaction of cells with the underlying matrix can be studied with various approaches that enable the simultaneous tracking of cellular dynamics and surface changes: well-known examples include surface micropatterning,[59] surface and cell labeling,[60] and the use of different imaging modes.[61] In this study, we developed a new method involving light microscopy, SEM, and AFM that enabled us to overlay images of cell dynamics on bone, a natural substrate whose complex and heterogeneous morphology requires imaging techniques that can resolve local characteristics at the submicron level.

The need to maintain the substrate in as close to physiological conditions as possible required imaging under ambient conditions, avoiding bone drying or manipulation of any kind. Two main tools were crucial to our successful solution: the correlative holder made it possible to keep the bone surface hydrated and in place throughout the experimental sequence, and the airSEM imaging station served to bridge between live dynamic tracking of cells and electron

DOI: 10.1021/acsami.5b08126
ACS Appl. Mater. Interfaces XXXX, XXX, XXX−XXX

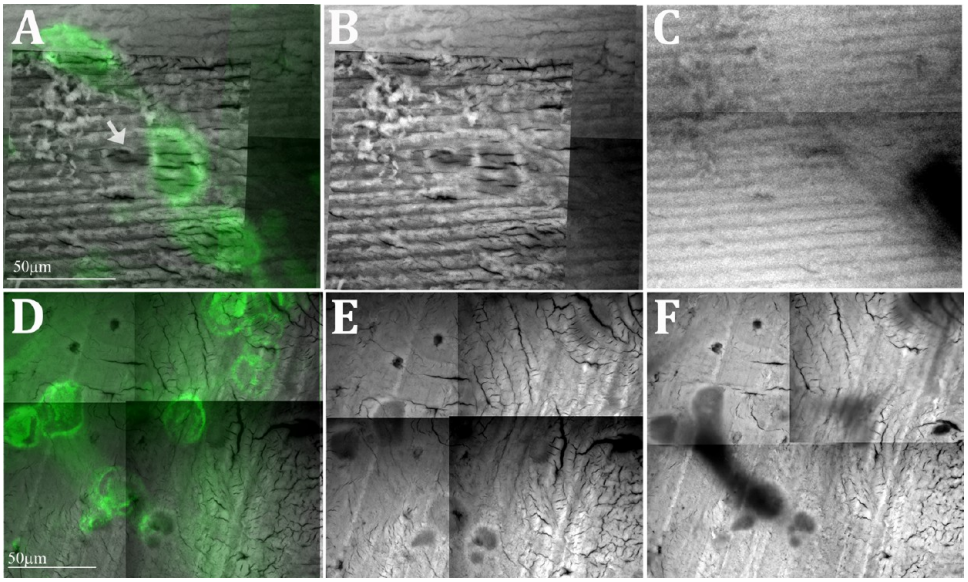

Figure 6. Osteoclast resorption of bone surface and its relation to SZ rings. (A) Overlay of rings in osteoclasts, fixed 24 h post-transfer to bone, with the bone surface after cell removal, showing that the rings form above resorption pits matching in size and shape. One pit (arrow) appears to be unrelated to any SZ. (B) The bone surface following cell removal [shown overlaid with rings in (A)], displaying the exposed resorption pits. (C) The same bone surface prior to cell transfer, decorated by saw markings. Comparison of (B) and (C) shows that the pits, which correlate with SZ ring location, were not present prior to osteoclast interaction with bone. (D) Overlay of SZ rings in a cell fixed 48 h post-transfer to bone (green) overlaid with images of the bone surface, following cell removal. (E) Resorption pits, seen after cell removal. The pits correlate to the SZ rings in (D). (F) airSEM image of the surface with the osteoclast still present, creating a shadow on the surface. The NaOCl treatment to remove the cells [compare (E) and (F)] causes some widening of cracks that were present before but otherwise does not modify the bone surface.

imaging, producing SEM images, and enabling elemental analysis under ambient conditions, without damaging the bone surface.

The combination of AFM and SEM provides information on the physical and structural characteristics of bone at sufficient spatial resolution. To further understand the role of other potentially relevant parameters, such as local surface composition, or the presence of specific proteins, observations with complementary correlative imaging techniques (e.g., immunofluorescence labeling of the matrix) can be performed.

The in vitro approach that we developed entailed use of cortical bone slices. The differences between these substrates and the living tissue that cortical osteoclasts encounter in vivo are manifold: mainly, signaling is not mediated by osteocytes and other cells, and the topography is artificially created. However, even within those limits, the devitalized bone surfaces preserve the basic bone structure, enabling us to study the effects of relevant structural features on osteoclast adhesion and resorption.

In our preliminary study of osteoclast adhesion to the bone surface, overlaying images of SZ rings with images of the bone surface, both prior to and following cell interactions with the surface, demonstrated a clear correlation between surface features and SZ rings, the latter adapting the feature's size and shape. The diameter of SZ rings formed, starting from the early stages of osteoclast adhesion, surrounding bulges on the bone surface was 7.5 μm in average (Figure 2). The measured height of such bulge, associated with the formation of small SZ rings was 1.3 μm (Figure 3). The observed preference of SZ rings to form around features that are comparable in their dimensions to several podosomes, suggests that these dimensions stabilize the SZ rings; this stabilization may result in longer ring lifetimes (Figure 5) and eventually in resorption. The observation that resorption pits were developed only at longer times (from 24 h post cell transfer) and were seen only in relation to larger SZ rings (diameter of 31 μm; see Figure 6) can point to the correlated development of SZ and resorption functionality of osteoclasts with time and needs to be further confirmed. At the micrometer scale, the mechanism underlying SZ stabilization and adaptation to the surface topography can be further examined by dynamically tracking SZ progression with live fluorescence imaging (step 5 in Scheme 1), and comparing it to local surface topography before and after cell interaction (steps 3 and 8 in Scheme 1, respectively). In contrast to the bulges, SZ rings did not preferentially associate with physiologically relevant structures displaying negative topography, such as osteocyte lacunas and microcracks. A similar phenomenon was also observed on dentin slices.[62] It is, however, possible that during cell interactions, structures with negative topography were filled with organic material, masking their interaction with the SZ rings.

The correlative imaging method that we developed is flexible, and it can be adapted to combine various imaging modalities and analysis tools (some of which were already put in practice in this work) to address a variety of different questions that require correlative approach in the field of cell sensing and related modification of the ECM. It is possible to apply it on different substrates relevant to cellular adhesion and function; specifically, in the field of bone implants the evaluation of the proposed implant design requires SEM imaging for compositional and topographic characterization,[31,63] indentation to examine the mechanical properties,[64,65] and imaging of fixed adherent cells[29] to evaluate cellular response and the chances of successful osseointegration.[66] Our developed strategy can provide a useful means for the combined assessment of these features. The compositional, structural, mechanical, and topographic properties of the implant of interest can be visualized before, after, and in relation to osteoblast or

DOI: 10.1021/acsami.5b08126
ACS Appl. Mater. Interfaces XXXX, XXX, XXX−XXX

osteoclast dynamic response. This may include adhesion, migration, and remodeling functionalities. Subsequent to the analysis, the surfaces could then be modified at the micrometer level, eventually providing better design of the implant.

SUMMARY AND CONCLUSIONS

We designed, constructed, and applied here a correlative, noninvasive technique for the parallel acquisition of live dynamic observations and high-resolution surface characterization in biological environments. In relation to osteoclast function, SZ rings imaged with live cell microscopy could be directly correlated to the local properties of the underlying bone surface and its modification. Rapid imaging in ambient conditions further enabled us to scan areas of several square millimeters, on which many cells can be simultaneously tracked. The ability developed here to connect changes in surface properties to specific cellular and subcellular dynamics can be conceivably applied to study a variety of relevant questions in the field of cell−matrix interaction.

ASSOCIATED CONTENT

Supporting Information

The Supporting Information is available free of charge on the ACS Publications website at DOI: 10.1021/acsami.5b08126.

EDX data obtained from a polished bone surface, high-resolution SEM images of bone resorption, fluorescence images of osteoclasts fixed after transfer to bone surface, correlation between SZ rings and the bone surface after cell removal, and bone surface area of interest, imaged by the airSEM and ESEM following osteoclast removal. (PDF)

Video illustration of dynamic ring sizes and stability. (AVI)

AUTHOR INFORMATION

Corresponding Author

*E-mail: Lia.Addadi@weizmann.ac.il. Phone: +972-8-934 2228.

Notes

The authors declare no competing financial interest.

ACKNOWLEDGMENTS

We thank I. Kaplan-Ashiri from the Weizmann Institute EM Center for help with ESEM imaging; B. Pasmantirer from the Instruments Design Section at the Weizmann Institute for designing the correlative holder; Y. Brami from B-Nano for assistance with bone imaging; the lab of R. Shahar for assistance with bone cutting; Y. Halfin and T. Levi from "Moo&Moo" for supplying of fresh cattle femur according to our specifications; B. Morgenstern for her skilled style editing of the manuscript. The authors wish to acknowledge the support provided to L.A. by the Schmidt Minerva Center and the Jeanne and Joseph Nissim Foundation for Life Sciences Research, and to B.G. by the ERC Project (294852, SynAd) and the Israel Science Foundation. L.A.is the incumbent of the Dorothy and Patrick Gorman Professorial Chair of Biological Ultrastructure; B.G is the incumbent of the Erwin Neter Professorial Chair in Cell and Tumor Biology.

ABBREVIATIONS

AFM, atomic force microscopy
CLEM, correlative light electron microscopy
GFP, green fluorescent protein
ESEM, environmental scanning electron microscopy
SEM, scanning electron microscopy
SZ, sealing zone

REFERENCES

(1) Parfitt, A. M. The Coupling of Bone Formation to Bone Resorption: A Critical Analysis of the Concept and of its Relevance to the Pathogenesis of Osteoporosis. *Metab. Bone Dis. Relat. Res.* **1982**, *4*, 1−6.

(2) Frost, H. M. Bone "Mass" and the "Mechanostat": A Proposal. *Anat. Rec.* **1987**, *219*, 1−9.

(3) Martin, T. J.; Seeman, E. Bone Remodelling: its Local Regulation and the Emergence of Bone Fragility. *Best Pract Res. Clin Endocrinol Metab* **2008**, *22*, 701−722.

(4) Henriksen, K.; Neutzsky-Wulff, A. V.; Bonewald, L. F.; Karsdal, M. A. Local Communication on and within Bone Controls Bone Remodeling. *Bone* **2009**, *44*, 1026−1033.

(5) Hazenberg, J. G.; Hentunen, T. A.; Heino, T. J.; Kurata, K.; Lee, T. C.; Taylor, D. Microdamage Detection and Repair in Bone: Fracture Mechanics, Histology, Cell Biology. *Technol. Health Care* **2009**, *17*, 67−75.

(6) Mulcahy, L. E.; Taylor, D.; Lee, T. C.; Duffy, G. P. RANKL and OPG Activity is Regulated by Injury Size in Networks of Osteocyte-like Cells. *Bone* **2011**, *48*, 182−188.

(7) Lanyon, L. E.; Sugiyama, T.; Price, J. S. Regulation of Bone Mass: Local Control or Systemic Influence or Both? *IBMS BoneKEy* **2009**, *6*, 218−226.

(8) Verborgt, O.; Gibson, G. J.; Schaffler, M. B. Loss of Osteocyte Integrity in Association with Microdamage and Bone Remodeling after Fatigue in vivo. *J. Bone Miner. Res.* **2000**, *15*, 60−67.

(9) Tan, S. D.; de Vries, T. J.; Kuijpers-Jagtman, A. M.; Semeins, C. M.; Everts, V.; Klein-Nulend, J. Osteocytes Subjected to Fluid Flow Inhibit Osteoclast Formation and Bone Resorption. *Bone* **2007**, *41*, 745−751.

(10) Xiong, J.; Onal, M.; Jilka, R. L.; Weinstein, R. S.; Manolagas, S. C.; O'Brien, C. A. Matrix-Embedded Cells Control Osteoclast Formation. *Nat. Med.* **2011**, *17*, 1235−1241.

(11) Takahashi, H.; Hattner, R.; Epker, B. N.; Frost, H. M. Evidence that Bone Resorption Precedes Formation at the Cellular Level. *Henry Ford Hosp Med. Bull.* **1964**, *12*, 359−364.

(12) Mulari, M. T.; Qu, Q.; Harkonen, P. L.; Vaananen, H. K. Osteoblast-Like Cells Complete Osteoclastic Bone Resorption and Form New Mineralized Bone Matrix in vitro. *Calcif. Tissue Int.* **2004**, *75*, 253−261.

(13) Delaisse, J. M. The Reversal Phase of the Bone-Remodeling Cycle: Cellular Prerequisites for Coupling Resorption and Formation. *BoneKEy Rep.* **2014**, *3*, 1−8.

(14) Weiner, S.; Traub, W. Bone Structure: from Angstroms to Microns. *FASEB J.* **1992**, *6*, 879−885.

(15) Black, J.; Mattson, R.; Korostoff, E. Haversian Osteons: Size, Distribution, Internal Structure, and Orientation. *J. Biomed. Mater. Res.* **1974**, *8*, 299−319.

(16) Block, M. R.; Badowski, C.; Millon-Fremillon, A.; Bouvard, D.; Bouin, A.-P.; Faurobert, E.; Gerber-Scokaert, D.; Planus, E.; Albiges-Rizo, C. Podosome-Type Adhesions and Focal Adhesions, So Alike Yet So Different. *Eur. J. Cell Biol.* **2008**, *87*, 491−506.

(17) Linder, S.; Aepfelbacher, M. Podosomes: Adhesion Hot-Spots of Invasive Cells. *Trends Cell Biol.* **2003**, *13*, 376−385.

(18) Destaing, O.; Saltel, F.; Geminard, J. C.; Jurdic, P.; Bard, F. Podosomes Display Actin Turnover and Dynamic Self-Organization in Osteoclasts Expressing Actin-Green Fluorescent Protein. *Mol. Biol. Cell* **2003**, *14*, 407−416.

(19) Saltel, F.; Chabadel, A.; Bonnelye, E.; Jurdic, P. Actin Cytoskeletal Organisation in Osteoclasts: A Model to Decipher Transmigration and Matrix Degradation. *Eur. J. Cell Biol.* **2008**, *87*, 459−468.

DOI: 10.1021/acsami.5b08126
ACS Appl. Mater. Interfaces XXXX, XXX, XXX−XXX

(20) Pfaff, M.; Jurdic, P. Podosomes in Osteoclast-like Cells Structural Analysis and Cooperative Roles of Paxillin, Proline-Rich Tyrosine Kinase 2 (Pyk2) and Integrin $\alpha V\beta 3$. *J. Cell Sci.* **2001**, *114*, 2775−2786.
(21) Helfrich, M.; Nesbitt, S.; Lakkakorpi, P.; Barnes, M.; Bodary, S.; Shankar, G.; Mason, W.; Mendrick, D.; Väänänen, H.; Horton, M. β_1 Integrins and Osteoclast Function: Involvement in Collagen Recognition and Bone Resorption. *Bone* **1996**, *19*, 317−328.
(22) van den Dries, K.; Schwartz, S. L.; Byars, J.; Meddens, M. B.; Bolomini-Vittori, M.; Lidke, D. S.; Figdor, C. G.; Lidke, K. A.; Cambi, A. Dual-Color Superresolution Microscopy Reveals Nanoscale Organization of Mechanosensory Podosomes. *Mol. Biol. Cell* **2013**, *24*, 2112−2123.
(23) Blair, H. C.; Yaroslavskiy, B. B.; Robinson, L. J.; Mapara, M. Y.; Pangrazio, A.; Guo, L.; Chen, K.; Vezzoni, P.; Tolar, J.; Orchard, P. J. Osteopetrosis with Micro-Lacunar Resorption Because of Defective Integrin Organization. *Lab. Invest.* **2009**, *89*, 1007−1017.
(24) Hirvonen, M. J.; Fagerlund, K.; Lakkakorpi, P.; Vaananen, H. K.; Mulari, M. T. Novel Perspectives on the Transcytotic Route in Osteoclasts. *BoneKEy Rep.* **2013**, *2*, 1−8.
(25) Mulari, M.; Vääräniemi, J.; Väänänen, H. K. Intracellular Membrane Trafficking in Bone Resorbing Osteoclasts. *Microsc. Res. Tech.* **2003**, *61*, 496−503.
(26) Coxon, F. P.; Thompson, K.; Roelofs, A. J.; Ebetino, F. H.; Rogers, M. J. Visualizing Mineral Binding and Uptake of Bisphosphonate by Osteoclasts and Non-Resorbing Cells. *Bone* **2008**, *42*, 848−860.
(27) Geblinger, D.; Zink, C.; Spencer, N. D.; Addadi, L.; Geiger, B. Effects of Surface Microtopography on the Assembly of the Osteoclast Resorption Apparatus. *J. R. Soc., Interface* **2012**, *9*, 1599−1608.
(28) Geblinger, D.; Addadi, L.; Geiger, B. Nano-Topography Sensing by Osteoclasts. *J. Cell Sci.* **2010**, *123*, 1503−1510.
(29) Duplat, D.; Chabadel, A.; Gallet, M.; Berland, S.; Bédouet, L.; Rousseau, M.; Kamel, S.; Milet, C.; Jurdic, P.; Brazier, M.; Lopez, E. The in vitro Osteoclastic Degradation of Nacre. *Biomaterials* **2007**, *28*, 2155−2162.
(30) Marchisio, M.; Di Carmine, M.; Pagone, R.; Piattelli, A.; Miscia, S. Implant Surface Roughness Influences Osteoclast Proliferation and Differentiation. *J. Biomed. Mater. Res., Part B* **2005**, *75*, 251−256.
(31) Deligianni, D. D.; Katsala, N.; Ladas, S.; Sotiropoulou, D.; Amedee, J.; Missirlis, Y. F. Effect of Surface Roughness of the Titanium Alloy Ti−6Al−4V on Human Bone Marrow Cell Response and on Protein Adsorption. *Biomaterials* **2001**, *22*, 1241−1251.
(32) Saltel, F.; Destaing, O.; Bard, F.; Eichert, D.; Jurdic, P. Apatite-Mediated Actin Dynamics in Resorbing Osteoclasts. *Mol. Biol. Cell* **2004**, *15*, 5231−5241.
(33) Shimizu, H.; Sakamoto, S.; Sakamoto, M.; Lee, D. D. The Effect of Substrate Composition and Condition on Resorption by Isolated Osteoclasts. *Bone Miner.* **1989**, *6*, 261−275.
(34) Nakamura, I.; Takahashi, N.; Sasaki, T.; Jimi, E.; Kurokawa, T.; Suda, T. Chemical and Physical Properties of the Extracellular Matrix are Required for the Actin Ring Formation in Osteoclasts. *J. Bone Miner. Res.* **1996**, *11*, 1873−1879.
(35) Bozec, L.; Groot, J.; Odlyha, M.; Nicholls, B.; Nesbitt, S.; Flanagan, A.; Horton, M. Atomic Force Microscopy of Collagen Structure in Bone and Dentine Revealed by Osteoclastic Resorption. *Ultramicroscopy* **2005**, *105*, 79−89.
(36) Hefti, T.; Frischherz, M.; Spencer, N. D.; Hall, H.; Schlottig, F. A Comparison of Osteoclast Resorption Pits on Bone with Titanium and Zirconia Surfaces. *Biomaterials* **2010**, *31*, 7321−7331.
(37) Sodek, J.; McKee, M. D. Molecular and Cellular Biology of Alveolar Bone. *Periodontol. 2000* **2000**, *24*, 99−126.
(38) Bianco, P.; Fisher, L. W.; Young, M. F.; Termine, J. D.; Robey, P. G. Expression and Localization of the Two Small Proteoglycans Biglycan and Decorin in Developing Human Skeletal and Non-Skeletal Tissues. *J. Histochem. Cytochem.* **1990**, *38*, 1549−1563.
(39) Geblinger, D.; Geiger, B.; Addadi, L. Surface-Induced Regulation of Podosome Organization and Dynamics in Cultured Osteoclasts. *ChemBioChem* **2009**, *10*, 158−165.
(40) Kukulski, W.; Schorb, M.; Welsch, S.; Picco, A.; Kaksonen, M.; Briggs, J. A. Correlated Fluorescence and 3D Electron Microscopy with High Sensitivity and Spatial Precision. *J. Cell Biol.* **2011**, *192*, 111−119.
(41) Kopek, B. G.; Shtengel, G.; Xu, C. S.; Clayton, D. A.; Hess, H. F. Correlative 3D Superresolution Fluorescence and Electron Microscopy Reveal the Relationship of Mitochondrial Nucleoids to Membranes. *Proc. Natl. Acad. Sci. U. S. A.* **2012**, *109*, 6136−6141.
(42) Revach, O. Y.; Weiner, A.; Rechav, K.; Sabanay, I.; Livne, A.; Geiger, B. Mechanical Interplay Between Invadopodia and the Nucleus in Cultured Cancer Cells. *Sci. Rep.* **2015**, *5*, 1−13.
(43) Monserrate, A.; Casado, S.; Flors, C. Correlative Atomic Force Microscopy and Localization-Based Super-Resolution Microscopy: Revealing Labelling and Image Reconstruction Artefacts. *ChemPhysChem* **2014**, *15*, 647−650.
(44) Puech, P. H.; Poole, K.; Knebel, D.; Muller, D. J. A New Technical Approach to Quantify Cell−Cell Adhesion Forces by AFM. *Ultramicroscopy* **2006**, *106*, 637−644.
(45) Hassenkam, T.; Jørgensen, H. L.; Lauritzen, J. B. Mapping the Imprint of Bone Remodeling by Atomic Force Microscopy. *Anat. Rec., Part A* **2006**, *288*, 1087−1094.
(46) Wallace, J. M. Applications of Atomic Force Microscopy for the Assessment of Nanoscale Morphological and Mechanical Properties of Bone. *Bone* **2012**, *50*, 420−427.
(47) Mosekilde, L. Consequences of the Remodelling Process for Vertebral Trabecular Bone Structure: A Scanning Electron Microscopy Study (Uncoupling of Unloaded Structures). *Bone Miner.* **1990**, *10*, 13−35.
(48) Vashishth, D.; Tanner, K. E.; Bonfield, W. Contribution, Development and Morphology of Microcracking in Cortical Bone during Crack Propagation. *J. Biomech* **2000**, *33*, 1169−1174.
(49) Perdikouri, C.; Tagil, M.; Isaksson, H. Characterizing the Composition of Bone Formed During Fracture Healing Using Scanning Electron Microscopy Techniques. *Calcif. Tissue Int.* **2015**, *96*, 11−17.
(50) Kleinhans, C.; Schmid, F. F.; Schmid, F. V.; Kluger, P. J. Comparison of Osteoclastogenesis and Resorption Activity of Human Osteoclasts on Tissue Culture Polystyrene and on Natural Extracellular Bone Matrix in 2D and 3D. *J. Biotechnol.* **2015**, *205*, 101−110.
(51) Luxenburg, C.; Addadi, L.; Geiger, B. The Molecular Dynamics of Osteoclast Adhesions. *Eur. J. Cell Biol.* **2006**, *85*, 203−211.
(52) Schneider, C. A.; Rasband, W. S.; Eliceiri, K. W. NIH Image to ImageJ: 25 Years of Image Analysis. *Nat. Methods* **2012**, *9*, 671−675.
(53) Solomonov, I.; Talmi-Frank, D.; Milstein, Y.; Addadi, S.; Aloshin, A.; Sagi, I. Introduction of Correlative Light and airSEMTM Microscopy Imaging for Tissue Research Under Ambient Conditions. *Sci. Rep.* **2014**, *4*, 1−7.
(54) Horcas, I.; Fernandez, R.; Gomez-Rodriguez, J. M.; Colchero, J.; Gomez-Herrero, J.; Baro, A. M. WSXM: A Software for Scanning Probe Microscopy and a Tool for Nanotechnology. *Rev. Sci. Instrum.* **2007**, *78*, 13705−13708.
(55) Vidavsky, N.; Addadi, S.; Mahamid, J.; Shimoni, E.; Ben-Ezra, D.; Shpigel, M.; Weiner, S.; Addadi, L. Initial Stages of Calcium Uptake and Mineral Deposition in Sea Urchin Embryos. *Proc. Natl. Acad. Sci. U. S. A.* **2014**, *111*, 39−44.
(56) Jowsey, J. Studies of Haversian Systems in Man and Some Animals. *J. Anat.* **1966**, *100*, 857−864.
(57) Buckwalter, J.; Glimcher, M.; Cooper, R.; Recker, R. Bone Biology. *J. Bone Joint Surg Am.* **1995**, *77*, 1256−1275.
(58) Clarke, B. Normal Bone Anatomy and Physiology. *Clin. J. Am. Soc. Nephrol.* **2008**, *3*, 131−139.
(59) Balaban, N. Q.; Schwarz, U. S.; Riveline, D.; Goichberg, P.; Tzur, G.; Sabanay, I.; Mahalu, D.; Safran, S.; Bershadsky, A.; Addadi, L.; Geiger, B. Force and Focal Adhesion Assembly: A Close Relationship Studied Using Elastic Micropatterned Substrates. *Nat. Cell Biol.* **2001**, *3*, 466−472.

DOI: 10.1021/acsami.5b08126
ACS Appl. Mater. Interfaces XXXX, XXX, XXX−XXX

(60) Salo, J.; Lehenkari, P.; Mulari, M.; Metsikko, K.; Vaananen, H. K. Removal of Osteoclast Bone Resorption Products by Transcytosis. *Science* **1997**, *276*, 270−273.
(61) Petroll, W. M.; Ma, L. Direct, Dynamic Assessment of Cell-Matrix Interactions Inside Fibrillar Collagen Lattices. *Cell Motil. Cytoskeleton* **2003**, *55*, 254−264.
(62) Rumpler, M.; Würger, T.; Roschger, P.; Zwettler, E.; Peterlik, H.; Fratzl, P.; Klaushofer, K. Microcracks and Osteoclast Resorption Activity In Vitro. *Calcif. Tissue Int.* **2012**, *90*, 1−9.
(63) Pelled, G.; Tai, K.; Sheyn, D.; Zilberman, Y.; Kumbar, S.; Nair, L. S.; Laurencin, C. T.; Gazit, D.; Ortiz, C. Structural and Nanoindentation Studies of Stem Cell-based Tissue-Engineered Bone. *J. Biomech* **2007**, *40*, 399−411.
(64) Bao, M.; Lou, X.; Zhou, Q.; Dong, W.; Yuan, H.; Zhang, Y. Electrospun Biomimetic Fibrous Scaffold from Shape Memory Polymer of PDLLA-co-TMC for Bone Tissue Engineering. *ACS Appl. Mater. Interfaces* **2014**, *6*, 2611−2621.
(65) Li, L.; Zuo, Y.; Zou, Q.; Yang, B.; Lin, L.; Li, J.; Li, Y. Hierarchical Structure and Mechanical Improvement of an n-HA/GCO−PU Composite Scaffold for Bone Regeneration. *ACS Appl. Mater. Interfaces* **2015**, *7*, 22618−22629.
(66) von Wilmowsky, C.; Moest, T.; Nkenke, E.; Stelzle, F.; Schlegel, K. A. Implants in Bone: Part II. Research on Implant Osseointegration: Material Testing, Mechanical Testing, Imaging and Histoanalytical Methods. *Oral Maxillofac Surg* **2014**, *18*, 355−372.

DOI: 10.1021/acsami.5b08126
ACS Appl. Mater. Interfaces XXXX, XXX, XXX−XXX